Nanoelectronics and Its New Materials – A NEW ERA OF NANOSCIENCE

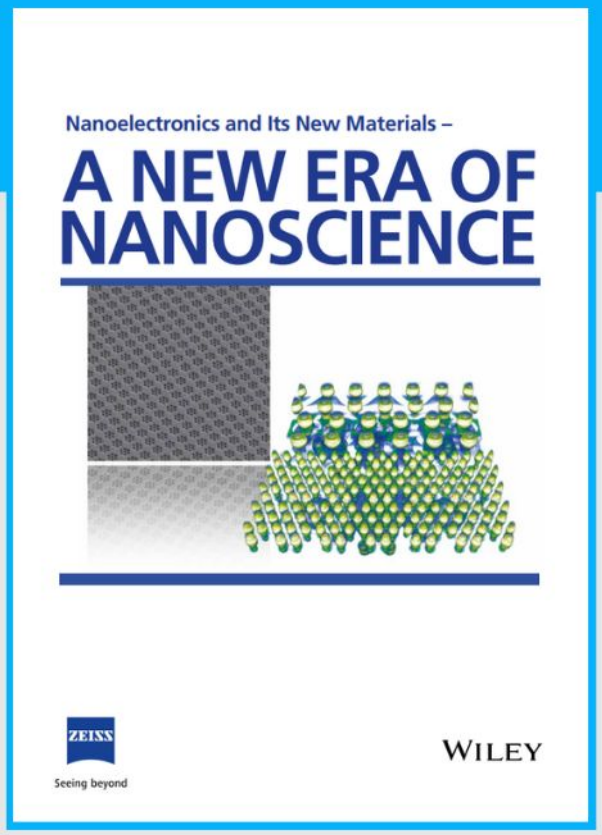

Discover the recent advances in electronics research and fundamental nanoscience.

Nanotechnology has become the driving force behind breakthroughs in engineering, materials science, physics, chemistry, and biological sciences. In this compendium, we delve into a wide range of novel applications that highlight recent advances in electronics research and fundamental nanoscience. From surface analysis and defect detection to tailored optical functionality and transparent nanowire electrodes, this eBook covers key topics that will revolutionize the future of electronics.

To get your hands on this valuable resource and unleash the power of nanotechnology, simply download the eBook now. Stay ahead of the curve and embrace the future of electronics with nanoscience as your guide.

ZEISS

Seeing beyond

WILEY

NANO · MICRO small
www.small-journal.com

Electronic Structure of Colloidal 2H-MoS_2 Mono and Bilayers Determined by Spectroelectrochemistry

*Kai M. Wurst, Onno Strolka, Jonas Hiller, Jakob Keck, Alfred J. Meixner, Jannika Lauth, and Marcus Scheele**

The electronic structure of mono and bilayers of colloidal 2H-MoS_2 nanosheets synthesized by wet-chemistry using potential-modulated absorption spectroscopy (EMAS), differential pulse voltammetry, and electrochemical gating measurements is investigated. The energetic positions of the conduction and valence band edges of the direct and indirect bandgap are reported and observe strong bandgap renormalization effects, charge screening of the exciton, as well as intrinsic n-doping of the as-synthesized material. Two distinct transitions in the spectral regime associated with the C exciton are found, which overlap into a broad signal upon filling the conduction band. In contrast to oxidation, the reduction of the nanosheets is largely reversible, enabling potential applications for reductive electrocatalysis. This work demonstrates that EMAS is a highly sensitive tool for determining the electronic structure of thin films with a few nanometer thicknesses and that colloidal chemistry affords high-quality transition metal dichalcogenide nanosheets with an electronic structure comparable to that of exfoliated samples.

1. Introduction

Transition metal dichalcogenides (TMDCs), such as MoS_2, are 2D materials with exciting perspectives for application in (opto-)electronic devices[1] or catalysis.[2] Within the three known polytypes (1T, 2H, and 3R)[3] of this material, 2H-MoS_2 is of particular interest due to its semiconducting nature and thickness-dependent band gap.[4] Apart from the established synthetic pathways toward 2H-MoS_2 with defined layer thickness, including mechanical[5] or liquid[6] based exfoliation and chemical[7] as well as physical vapor deposition,[8] wet-chemical techniques affording colloidally stable TMDCs have recently emerged,[9–12] which are based on principles originally developed for the synthesis of colloidal quantum dots.[13] Some advantages of wet-chemically synthesized TMDCs are their scalability, relative ease of purification, and solution-processability, which render them particularly suitable for application in LEDs[14] or solar cells.[15] For these applications, detailed knowledge of the electronic structure, such as the exact position of the band edges, is crucial to design efficient device stacks, in which the layers of several materials, for example, electron-/hole-conducting and blocking layers, as well as the active layer, are electronically matched. Standard electrochemical investigations, such as cyclic voltammetry (CV)[16] or differential pulse voltammetry (DPV), can provide such information, which is much easier and usually faster to perform compared to ultraviolet photoelectron spectroscopy[17] or scanning tunneling spectroscopy[18] investigations. However, a shortcoming of standard electrochemical techniques is the lack of differentiation between band edges and trap states, which is only afforded by combining electrochemistry with optical spectroscopy. Such spectroelectrochemistry detects changes in the absorption or luminescence of a sample upon oxidation or reduction. This way, the band edges or energy levels involved in a specific optical transition can be identified by determining the potential at which this transition bleaches, either due to electron injection into the final state (reduction) or depletion of electrons in the initial state (oxidation). In contrast, reducing or oxidizing trap states will have a minor effect on the absorption spectrum, allowing for the distinction between band edges and trap states.

While the limited sensitivity of standard spectroelectrochemistry may be problematic for the investigation of thin films with few nanometer thicknesses,[19–21] Hickey et al. introduced potential-modulated absorption spectroscopy (EMAS),[22] which is sensitive enough to study monolayers of CdSe quantum dots.[23]

K. M. Wurst, O. Strolka, J. Hiller, J. Keck, A. J. Meixner, J. Lauth, M. Scheele
Institute of Physical and Theoretical Chemistry
University of Tübingen
Auf der Morgenstelle 18, 72076 Tübingen, Germany
E-mail: marcus.scheele@uni-tuebingen.de
O. Strolka, J. Lauth
Cluster of Excellence PhoenixD (Photonics, Optics and Engineering - Innovation Across Disciplines)
30167 Hannover, Germany
A. J. Meixner, J. Lauth, M. Scheele
Center for Light-Matter Interaction, Sensors & Analytics (LISA+)
University of Tübingen
Auf der Morgenstelle 15, 72076 Tübingen, Germany
J. Lauth
Laboratory of Nano and Quantum Engineering, LNQE
Leibniz Universität Hannover
30167 Hannover, Germany
The ORCID identification number(s) for the author(s) of this article can be found under https://doi.org/10.1002/smll.202207101.

DOI: 10.1002/smll.202207101

Using EMAS, DPV, and electrochemical gating (ECG)[24] experiments, we present here the electronic structure of colloidal 2H-MoS_2 nanosheets with a thickness of 1–2 monolayers and lateral size of 20–25 nm. We demonstrate that the novel wet-chemical pathway affords 2H-MoS_2 nanosheets of the same quality and unique electronic features as those previously described for 2H-MoS_2 films obtained by liquid exfoliation,[25] namely a direct bandgap, intrinsic n-doping, as well as strong bandgap renormalization upon doping.[26] We determine the exact energetic positions of the band edges involved in the direct transition, as well as those constituting the indirect transition in bilayers. We find strong indications for two distinct band nesting transitions and report the energetic position of the points in the conduction band edge involved in these. While oxidation of the 2H-MoS_2 is irreversible, we observe a mostly reversible reduction even for potentials far above the conduction band edge, rendering this material suitable for reductive electrocatalysis, for example, for electrocatalytic hydrogen evolution.

2. Results

2.1. Potential-Modulated Absorption Spectroscopy

Compared to standard spectroelectrochemistry, the lock-in amplifier-based EMAS technique achieves excellent sensitivity allowing to study thin films of 4 nm thickness or less. A more in-depth description of this measurement principle can be found elsewhere.[23,27] In short, a constant potential, located in the band gap at the open circuit potential (OCP), is applied to the transparent working electrode coated with the sample. This constant potential is modulated with periodic rectangular square pulses, such that a periodic redox potential is applied to the sample given by the amplitude of the square pulse. Simultaneously, the transmission of monochromatic, visible light through the working electrode is measured with a photodiode located behind the sample. A lock-in amplifier tuned to the frequency of the square pulse determines the potential-dependent absorption of the sample, from which the absolute value of a potential-dependent change in absorption ($|\Delta A|$) is obtained after subtracting the absorption at the OCP. Analyzing the phase relation between modulated potential and $|\Delta A|$ gives access to the sign of ΔA and allows identifying potential-dependent bleaches ($\Delta A < 0$) or induced absorptions ($\Delta A > 0$; see Figure S1, Supporting Information, and the associated text for details).

To facilitate this assignment, it is often useful to compare the EMAS spectrum with the steady-state absorption spectrum. **Figure 1**a depicts the steady-state absorption spectrum of colloidal 2H-MoS_2 nanosheets with a lateral size of 20–25 nm and a thickness of 1–2 monolayers deposited on a fluorine-doped tin oxide (FTO) substrate. For better visibility of the main optical transitions, we also plot the second derivative of the data. The A and B excitonic transitions are visible at 658 (1.88 eV) and 610 nm (2.03 eV), respectively. The prominent C exciton (or band nesting transition) occurs as a broad signal at 433 nm (2.86 eV) and a shoulder at 388 nm (3.20 eV). Utilizing the empirically found correlation between the number of monolayers per sheet N and A exciton wavelength λ_A,[6] $N = 2.3 \times 10^{36} \times \exp(-54888/\lambda_A)$, we anticipate an average layer thickness of 1.36 layers, which is in accordance with the TEM measurements in Figure 1b. Further complementary characterization of the 2H-MoS_2 nanosheets is provided in ref. [10] (X-ray diffraction, electron diffraction, FT-IR spectroscopy, photoelectron spectroscopy, and transient absorption), as well as by Raman spectroscopy in the Supporting Information. The clearly visible E^1_{2g} and A_{1g} Raman peaks indicate the 2H-phase of MoS_2, while their separation with a median of 21.7 cm^{-1} suggests a sample composed of few (mono-, bi-, or tri-) layer sheets of MoS_2 considering the 1 cm^{-1} energy resolution of this measurement.

Figure 2 displays the EMAS data of the same 1–2 monolayer 2H-MoS_2 nanosheets with an average film thickness of 138 nm on FTO measured in the reductive direction in 0.1 M n-Bu_4NPF_6/CH_3CN (the data of 4, 15, and 78 nm films is shown in Figures S4–S6, Supporting Information). Figure 2a–c shows linecuts of the wavelength-dependent ΔA at different reductive potentials, while Figure 2d depicts the whole dataset as a 2D spectrum. For better visibility of the changes at small potentials, Figure 2a–c shows the same data from the OCP at −0.5 V versus the Ferrocene/Ferrocenium redox couple (Fc/Fc^+) until a minimum potential of −1.1, −1.7, and −2.9 V versus Fc/Fc^+, respectively (from here on, all potentials are reported against

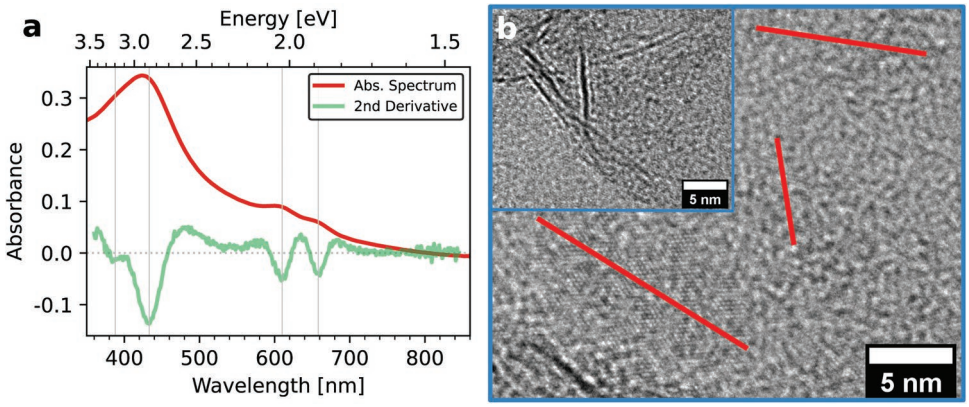

Figure 1. a) UV–vis spectrum of a 2H-MoS_2 nanosheet film deposited on FTO (red curve) and the second derivative of the data (green curve). b) TEM image of lying 2H-MoS_2 nanosheets. The lateral size is indicated by the red bars. The inset shows a picture of standing 2H-MoS_2 nanosheets.

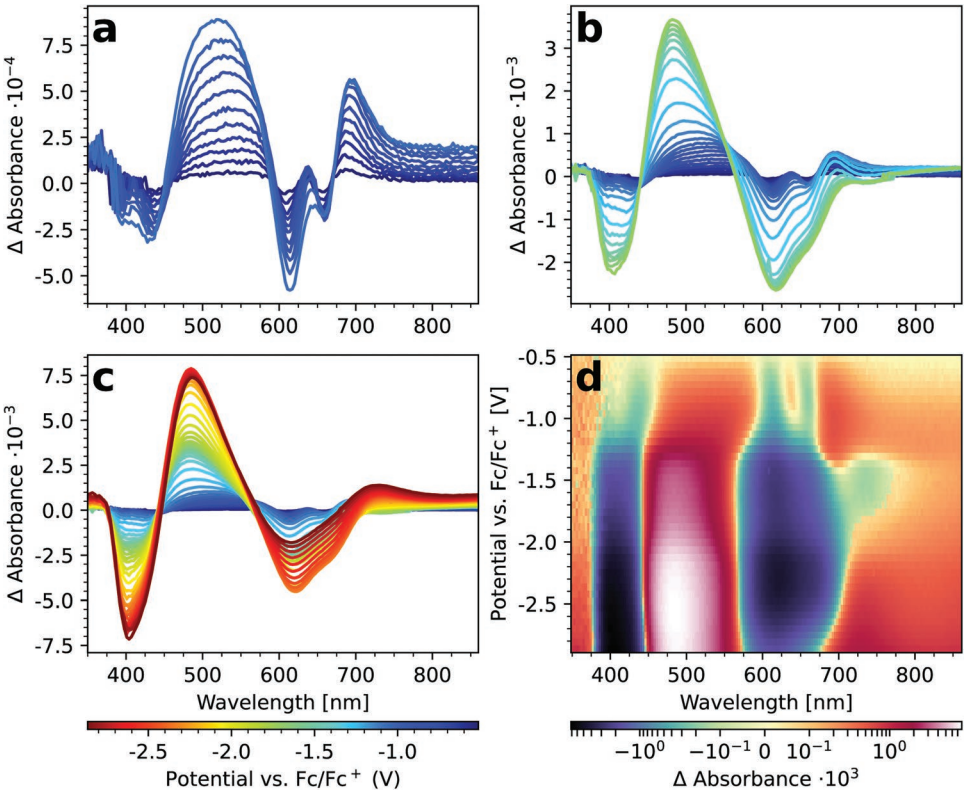

Figure 2. EMAS measurement of a 2H-MoS_2 nanosheet film with 138 nm average thickness in the reductive direction. Panels (a–c) depict the data until a minimum reductive potential of –1.1, –1.7, and –2.9 V versus Fc/Fc^+. Potentials are indicated by the color code. In (d) the whole dataset is shown as a contour plot whereby the change in absorbance is given by the respective color on the logarithmic color scale.

Fc/Fc^+). It should be noted that the FTO working electrode exhibits a potential-dependent ΔA itself (most notably at $\lambda > 750$ nm), but its magnitude is negligible compared to the EMAS signal of thick 2H-MoS_2 nanosheet films (cf. Figure S2, Supporting Information). We find a bleach of the A and B exciton as soon as the potential is increased above the OCP toward more reductive potentials (Figure 2a,b), where the bleach of the B exciton appears more pronounced than that of the A exciton. Further notable features for this reductive scan include the bleach of the C exciton and its shoulder (390–430 nm), an induced absorption at 700 nm, as well as a strong induced absorption between the C and A/B excitonic transitions. The maximum of this last signal shifts toward higher energies with more reductive potentials. Upon increasing the reductive potential above |–1.2 V|, the formerly clearly separated bleaches of the A/B exciton broaden and dissolve into a single feature (Figure 2c,d). We find that the change in ΔA is non-monotonous, which is why we depict the potential-dependent ΔA for selected wavelengths in **Figure 3**a. Most notably, the bleach of the A- and B-exciton exhibits two relative maxima at roughly –1.5 and –2.4 V. These maxima are even more clearly observed for thinner films, such as 15 nm (Figure 3b). The corresponding data of 78 and 4 nm films are shown in Figure S7, Supporting Information. Similar observations hold true for the bleach of the C exciton, as well as the induced absorption between the C and B excitons. The induced absorption at around 700 nm reaches a maximum of –1.1 V, after which it decreases again. We observe a small broad bleach with a minimum at 735–740 nm for potentials of –1.3 to –1.7 V, which transitions into a weak induced absorption for reductive potentials > |–2 V|.

In **Figure 4**, we scan a similar 138 nm thick 2H-MoS_2 nanosheet film on FTO in 0.1 M n-Bu_4NPF_6/CH_3CN into the oxidative direction from the OCP at –0.5 V toward +1.8 V and display the EMAS signal in the same manner as for the reductive direction in Figure 2. The most striking result is that the qualitative EMAS response is mostly inverse to the observations during the reductive scan. With increasing potential, slightly blue-shifted ($\Delta\lambda = 2$ nm) induced absorptions of equal intensity are seen for the A and B excitons. The C exciton shows a redshifted induced absorption at 434 nm, which is less pronounced compared to the signal in the reductive direction. Further notable features are a broad bleach with two components between the C and B exciton, a strong bleach at 690 nm, as well as another bleach between the A- and B-exciton. At wavelengths around 400 and >830 nm, the underlying signal of the FTO (cf. Figure S3, Supporting Information) substrate precludes an unambiguous analysis.

In **Figure 5**, we display the corresponding linecuts of ΔA versus the applied oxidative potential at the wavelength maxima of the A- and B-exciton. The trends are characteristic of all other features described above, as well as for films of varying thicknesses (see Figures S8–S11, Supporting Information). The ΔA changes immediately upon leaving the OCP and reaches a maximum at +1 V after which it monotonously decreases.

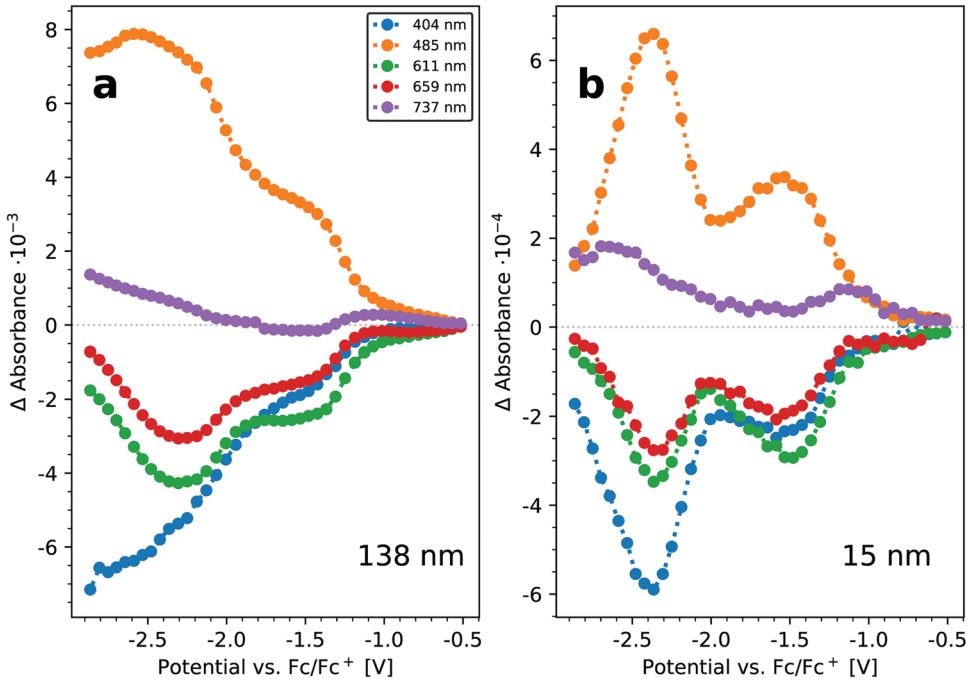

Figure 3. Linecuts of ΔA at different chosen wavelengths versus applied potential. In (a) for the reduction data of the 2H-MoS_2 nanosheet film with 138 nm average thickness shown in Figure 2 and in (b) for a film with 15 nm average thickness. The whole dataset of (b) is shown in Figure S5, Supporting Information.

2.2. Electrochemical Properties

To aid the interpretation of the EMAS experiments, we perform DPV and ECG measurements on the same colloidal 2H-MoS_2 nanosheets. DPV gives insights into the exact position of electronic states within the material including conduction/valence band and trap states. ECG allows drawing conclusions about the type of states (distinguishes between trap states and band edges) by measuring simultaneously the electrochemical density of states and the conductivity as a function of the applied potential.

2.2.1. Differential Pulse Voltammetry

Figure 6 depicts the DPV of the nanosheets in 0.1 M *n*-Bu_4NPF_6/CH_3CN on a Pt disc electrode (blue curves) against the background of the bare Pt electrode (orange curves). All measurements are initiated at the OCP of the uncoated electrode at –0.2 V and the electrochemical measurement window for this electrolyte is +1.8 to –2.8 V. In both scan directions, the current already starts to increase/decrease slightly in the vicinity of the OCP. In the oxidative direction, we observe a broad peak at 0.77 V including a shoulder at 0.37 V. At even more oxidative

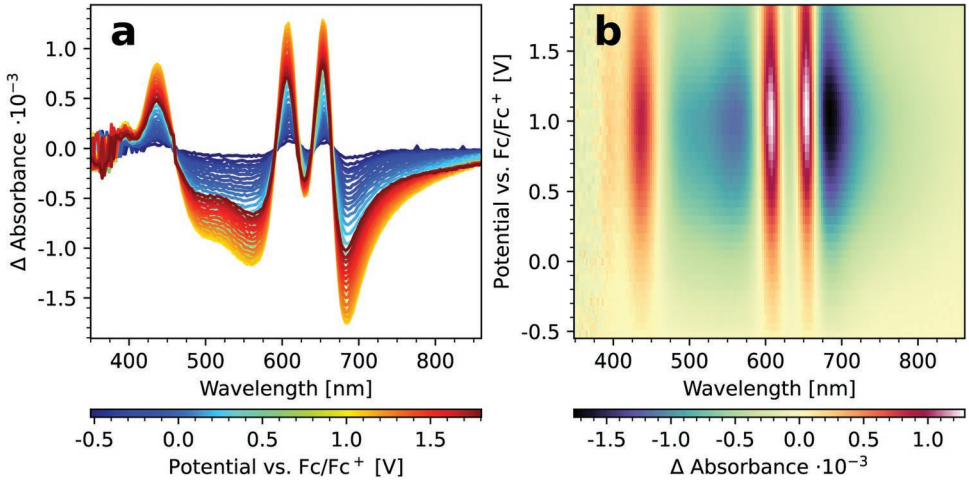

Figure 4. EMAS measurement of a 2H-MoS_2 nanosheet film with 138 nm average thickness in the oxidative direction. While both panels display the whole dataset, in (a) the potentials for the ΔA-spectra are indicated by the color code, where (b) shows a 2D contour plot comparable to Figure 2d.

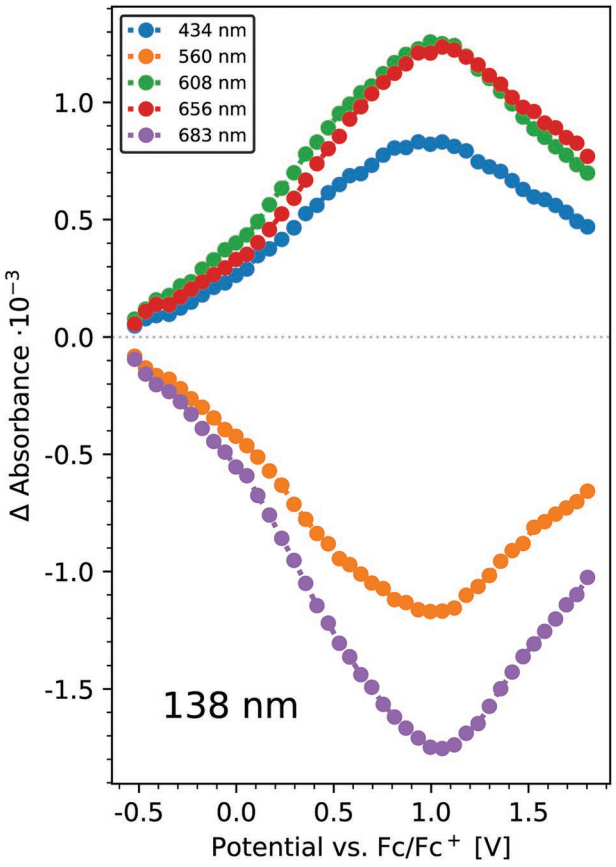

Figure 5. Linecuts of ΔA at different chosen wavelengths versus the applied potential for the oxidative EMAS scan of the 2H-MoS_2 nanosheet film with 138 nm average thickness shown in Figure 4.

potentials, the current increases further, however without a distinguishable feature. In the reductive direction, we find a small peak at –1.18 V and a prominent peak at –1.83 V. The intensity

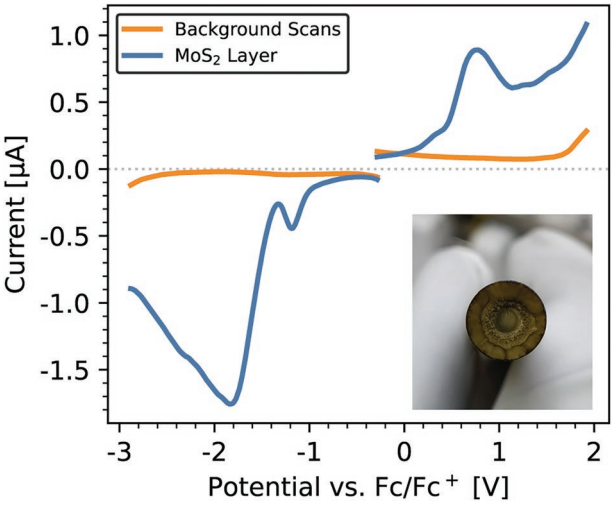

Figure 6. DPV measurements of the uncoated Pt disc electrode (orange) and the drop casted 2H-MoS_2 nanosheet film (blue) in the reductive and oxidative direction. The inset shows a photograph of the coated electrode.

of the second peak continuously drops toward more reductive potentials, but with a much flatter flank compared to the onset, suggesting that further reductive processes are buried within this signal.

2.2.2. Electrochemical Gating

ECG determines the potential-dependent conductivity, the differential capacitance, and the total injected charge. By measuring the amount of charge injected or withdrawn from the film within every single potential step, the differential capacitance contains information about the density of states. At the end of each potential step, the steady-state conductivity is measured, which allows the distinction between mobile or trapped charge carriers. The accumulated charge is determined by integrating the differential capacitance over the whole potential scan range, providing information on the reversibility of the charge injection.

Figure 7 shows the result of an ECG experiment for 161 nm thick 2H-MoS_2 nanosheet films deposited on Pt interdigitated electrodes and measured in 0.1 M *n*-Bu_4NPF_6/CH_3CN. Fresh films were prepared for each scan in the oxidative, as well as the reductive, scan direction. The left column (Figure 7a–c) shows two scans towards different reductive potentials, and the right column (Figure 7d–f) depicts one oxidative scan. The differential capacitance is shown in Figure 7a,d, the steady-state conductivity in Figure 7b,e, and the accumulated charge in Figure 7c,f. Forward scans, that is, measurements starting at the OCP at –0.5 V toward reductive or oxidative potentials, are shown as solid lines in each graph. The respective backward scans starting from the reductive or oxidative potential and going back to the OCP, are presented as dotted lines. For oxidative scans, we observe that both, the differential capacitance and the steady-state conductivity, change immediately. The differential capacitance starts to increase directly (Figure 7d), indicating an immediate removal of electrons, while the conductivity decreases (Figure 7e). At a potential of 0.25 V, the differential capacitance passes through a maximum and the conductivity drops more sharply. The differential capacitance continues to drop steadily up to higher potentials, while the conductivity falls almost to zero above the potential of about 0.8 V. During the back scan, we see clear signatures of an irreversible electrochemical process, specifically the negligible conductivity (Figure 7e, dotted line), a sluggish decrease in the number of the accumulated charge (Figure 7f, dotted line), and an unsymmetric differential capacitance compared to the forward scan (Figure 7d).

We find a fundamentally different behavior in the reductive direction. For maximum potentials below |–2.08 V|, a comparison of forward and backward scans suggests full electrochemical reversibility (Figure 7a, blue curve). Scanning to even more reductive potentials shifts the drop of the differential capacitance to higher potentials with each subsequent scan (see the shoulder forming in the red curve, which is a measurement that was performed after the film was reduced below –2.08 V several times), which is mirrored by the same behavior in the respective back scans (Figure 7a). In addition, the measurement at highly reductive potentials exhibits a shoulder at

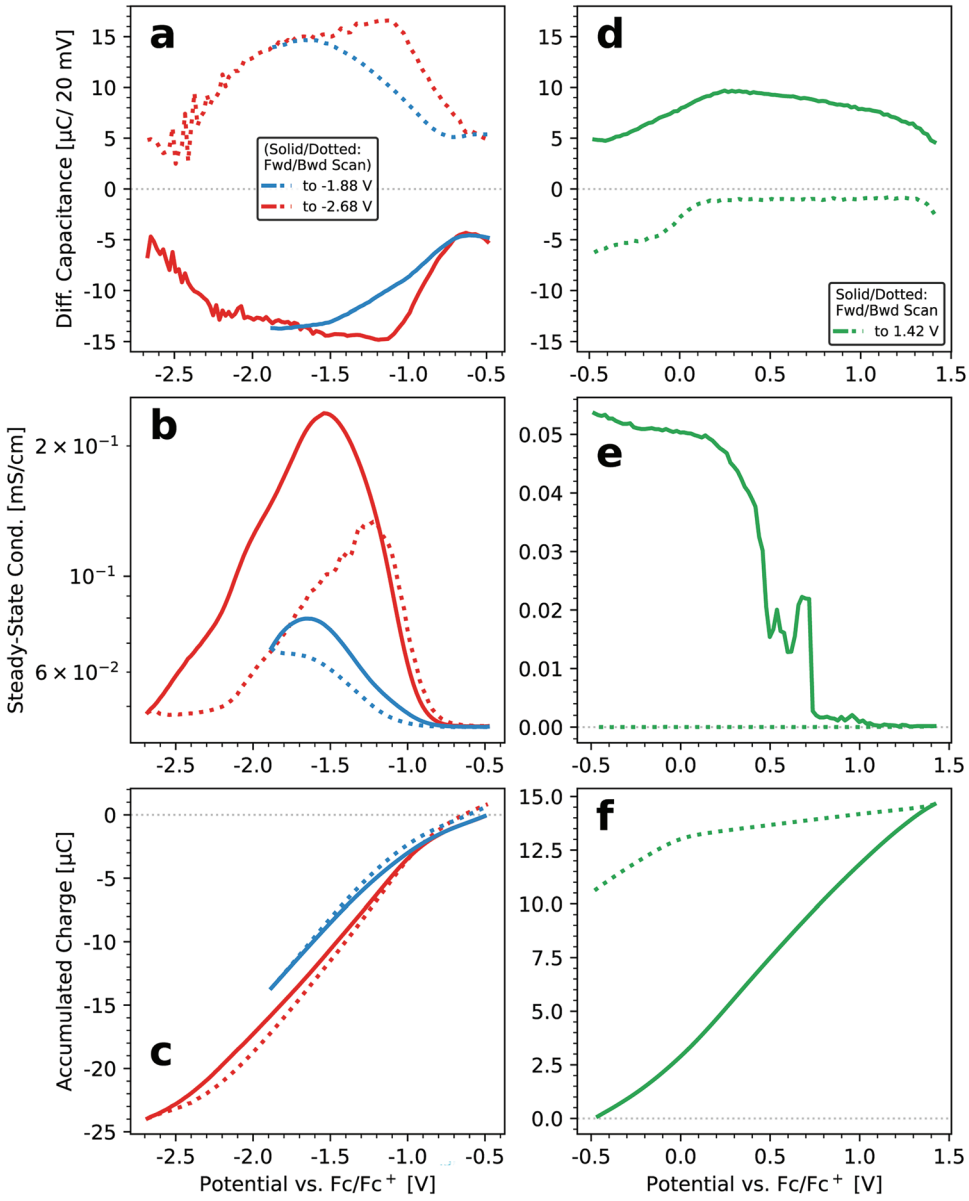

Figure 7. Electrochemical gating experiments of 161 nm thick 2H-MoS_2 nanosheet films deposited on Pt interdigitated electrodes in the reductive (left column) and oxidative (right column) scan direction. Forward scans are shown as solid and backward scans as dotted lines. Panels (a,d) depict the differential capacitance, panels (b,e) the steady-state conductivity, and panels (c,f) the accumulated charge. In the case of the reductive scan direction, one scan with a minimum reductive potential above (blue curve) and one below (red curve) −2 V versus Fc/Fc^+ are shown.

approximately −2 V in the forward and backward scans. We find comparable signs for electrochemical reversibility until −2.08 V in the steady-state conductivity (Figure 7b).

Identical to the oxidative scan direction, the samples exhibit an intrinsic conductivity at the OCP, which continuously increases with increasing reductive potential. Beyond −2.08 V, similar shifts of the onsets occur as in Figure 7a in conjunction with a notable overall increase in the conductivity by approximately doubling it. Analogous to the course of the differential capacitance, a shoulder arises at approx. −2 V versus Fc/Fc^+. During the back scans (dotted lines), the conductivity is smaller and no longer mirrors the forward scan. The accumulated charge (Figure 7c) also reflects this analysis. For reductive potentials below |−2.08 V|, the forward and back scans are identical, while a hysteresis occurs for more extended reductive scan windows. Comparable oxidative and reductive ECG scans of uncoated Pt IDE measured in 0.1 M *n*-Bu_4NPF_6/CH_3CN can be found in Figure S12, Supporting Information.

3. Discussion

Our comprehensive (spectro-)electrochemical analysis of colloidal 2H-MoS_2 nanosheets with a thickness of 1–2 layers and a lateral size of 20–25 nm affords the electronic structure shown in **Figure 8**. To approximate the corresponding energy values

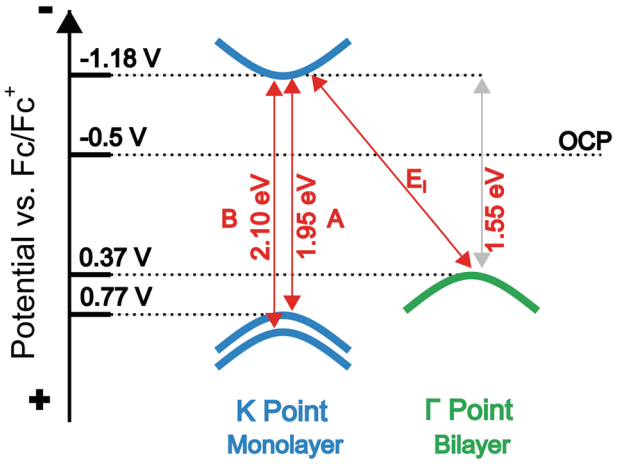

Figure 8. Energy scheme of mono and bilayer 2H-MoS_2 nanosheets together with their direct (A and B excitons) and indirect bandgap E_I, respectively. All indicated potentials are taken from the (spectro-)electrochemical analysis in this work. The OCP can be interpreted as the Fermi level.

with respect to the vacuum level, the reference value for the Ferrocene/Ferrocenium redox couple needs to be subtracted from the reported potentials. While different suggestions for this reference level exist,[28] we recommend the widely used value of −5.1 eV.

3.1. Determination of the Conduction Band Edge

We identify the potential of the conduction band edge with −1.2 V. This is inferred from the inflection point in EMAS at this potential (Figure 3) for the traces of the A- and B-exciton, as well as the first reductive peak in the DPV scan at −1.18 V (Figure 6). Utilizing points of inflection in EMAS for band edge localizations has been discussed before for CdSe quantum dots,[23,27] and the relatively weak DPV signal at the conduction band edge can be understood in terms of the low density of states at the K-point of the conduction band shown in previous theoretical calculations for monolayers.[29] Our assignment of the conduction band edge is also supported by the differential capacitance which exhibits reducible states at around −1.2 V (Figure 7a). The fusion of the formerly clearly resolved A- and B-exciton signals into a single broadband at −1.2 V (Figure 2d) is further evidence for reaching the band edge as a result of enhanced coulomb scattering of the excitons with free charge carriers.[30] We note that the conduction band edge for bulk 2H-MoS_2 at the K-point has been reported with −4.25 eV, which translates into approx. −0.85 V on the Fc/Fc^+ scale.[43]

3.2. Doping and Bandgap Renormalization

We note that the position of the OCP at −0.5 V, that is, only 0.7 V below the conduction band edge, indicates substantial n-doping of the nanosheets, which is supported by the immediate decrease of the steady-state conductivity upon oxidation (Figure 7e). We stress that bleaches of the A, B, and C excitons are instantaneously formed in the reductive EMAS scans upon departing from the OCP (Figure 2) even for potentials far below the conduction band edge. The bleaching below −1.2 V is therefore not caused by band filling but rather a sign of bandgap renormalization, previously observed in TA measurements,[10,31,32] by chemical doping[33] and by spectroelectrochemistry of 3-layer, 150 nm large 2H-MoS_2 nanosheets produced by liquid-based exfoliation.[25] Briefly, upon electron injection into 2H-MoS_2 nanosheets the self-energy of the electron and hole states decreases due to many-body effects, and this decrease is typically larger for the electron states.[26,30,34] If the concomitant decrease in excitonic binding energy (due to increased charge screening) is smaller than this band gap renormalization, a net red shift in absorption results from increased n-doping. Likewise, a net blueshift is expected for lowering the Fermi level. We, therefore, attribute the blue-shifted induced absorptions near the A/B-excitonic transitions during oxidation in Figure 4 to the same bandgap renormalization effect, given that it occurs immediately upon departing from the OCP.

3.3. Determination of the Valence Band Edge

Localizing the potential of the valence band edge is more challenging in view of the irreversible oxidation found for this material, which prevents an unambiguous determination of an inflection point in EMAS (Figure 5). Irreversible oxidation of 2H-MoS_2 has previously been reported,[16,35,36] and is most likely due to oxidation of Mo^{4+} to Mo^{6+}.[37] We interpret the pronounced oxidation peak in the DPV measurement at 0.77 V (Figure 6) as the valence band edge. This interpretation is further supported by the results of Padilha et al. who have shown that the valence band edges for monolayer and bilayer 2H-MoS_2 at K and Γ points, respectively, consist preferentially of contributions from the Mo d orbitals.[43] We hypothesize that the oxidation potential of holes in the valence band is strong enough to invoke the $Mo^{4+} \rightarrow Mo^{6+} + 2\ e^-$ oxidation. This agrees with the potential of 0.8 V during the oxidative ECG scan (Figure 7e) at which the conductivity vanishes almost completely. This finding can be rationalized with a compensation of the n-dopants, as well as the oxidative degradation, once the valence band edge is reached. It is also in reasonable agreement with the EMAS traces in Figure 5, considering that upon reaching the valence band, one would expect competition between induced absorption (due to band gap renormalization) and bleaching of the excitonic transitions (due to band filling).

3.4. Excitonic Binding Energy

From these considerations, we infer an electrochemical bandgap of ≈1.95 eV, which is less than 0.1 eV larger than the optical gap (note: the electrochemical bandgap is the difference of the potentials at which we find the oxidation of the valence band or reduction of the conduction band). Although this excitonic binding energy appears low for 2H-MoS_2, it is in line with the strong dependence of the excitonic binding energy on the dielectric constant of the surrounding medium.[38] In the present case, we may approximate the environment with pure

acetonitrile, which exhibits a very large dielectric constant of ≈35,[39] and thus, exerts strong dielectric screening for the electron–hole pair, which decreases the binding energy.

3.5. Location and Splitting of the C-Exciton

We find that the electrochemically induced bandgap renormalization probed for the A- and B-exciton (Figure 3, red and green trace) is also reflected in the potential-dependent absorption of the C-exciton (Figure 3, blue trace). While this may be fundamentally expected, it has not been previously demonstrated, and we speculate that its observation is facilitated by the much higher absorption intensity of the C transitions compared to the A and B transitions[6] in the laterally smaller 20–25 nm large 2H-MoS_2 nanosheets used in our experiments (e.g., compared to ref. [25]). Moreover, we find clear signs of two separate bleaches for the C-exciton between 390 and 430 nm (Figure 2a,b), which merge into a broad bleach at roughly –1.2 V. This is evidence for the theoretical prediction of two distinct band nesting features in MoS_2,[40] which has previously been confirmed for bulk 2H-MoS_2,[41] but, to the best of our knowledge, not for monolayer 2H-MoS_2. First insights in higher energy transitions of various monolayer TMDCs are reported by Hong et al., but no distinction between different contributions to the C band in 2H-MoS_2 was given.[42]

Although Figure 3 and the seemingly identical inflection points for the bleaching of the A/B- versus the C-excitons at –1.2 V may suggest that the involved electron states are identical, this is fundamentally impossible. The A/B excitons require a point in the Brillouin zone for which $\nabla_k E_C = 0$, while the definition of band nesting is $\nabla_k E_C \neq 0$ (and $\nabla_k E_C = \nabla_k E_V$).[40] Therefore, the involved electron states of the A/B-excitons versus the C-excitons must be located at different points in the Brillouin zone, but at roughly the same energy. Note that the corresponding hole state of the C excitons would be expected at a potential of >+1.7 V, which prevents its determination here due to the rapid degradation at such potentials.

3.6. Conduction and Valence Band Edges of the Indirect Transition

The analysis of the weak bleach at 735–740 nm in the potential range of –1.3 to –1.7 V (Figure 2 c,d) is complicated due to the adjacent induced absorption caused by the red-shifted A-exciton and overlapping induced absorption of FTO at wavelengths >750 nm. The most likely explanation for this EMAS band is the indirect transition inherent to 2H-MoS_2 with more than one monolayer.[25] Since we determined the average thickness of the nanosheets studied here with 1–2 monolayers, it is reasonable to assume that a significant portion of the sample will exhibit such an indirect transition. Computational studies have shown that for two layers of 2H-MoS_2, the electron state involved in the indirect transition is the same as that occupied by the A/B excitonic transitions.[41] The identical reductive potential at which we observe the bleaching of the A/B excitons and the transition at 730–740 nm, therefore, supports the assignment of the latter as the indirect transition. If this is correct, one would expect the corresponding hole state involved in the indirect transition at roughly +0.4 V. We note a small shoulder in the DPV measurement at 0.37 V (Figure 6), as well as a maximum in differential capacitance at 0.25 V in the forward scan of the ECG experiment (Figure 7d), which are both in line with this assignment. The energy difference between the direct and indirect transition of roughly 0.4 eV found here is in good agreement with the value predicted for bilayers by a computational study.[43]

Alternative explanations for the EMAS signal at 730–740 nm involve the formation of a trion,[44] as well as another direct transition at the H point, sometimes referred to as the A_H-exciton.[41] We argue that a trion is less likely here since its energy difference to the neutral exciton would be much larger than the previously measured value of 80 meV.[44] Similarly, the A_H-exciton would be expected to occur at an energy larger than the A-exciton, which is not the case here.[41]

3.7. Reversibility of Electrochemical Reduction

The colloidal 2H-MoS_2 nanosheets exhibit high stability under reductive conditions. For reductive potentials ≤ |–1.8 V|, the S-shape of the EMAS signal (Figure 3a), as well as the mostly hysteresis-free ECG data (Figure 7a–c), indicate almost complete electrochemical reversibility even for potentials that reach far out into the conduction band. The EMAS data contains a second inflection point at –2 V, which—once exceeded—marks a critical reductive potential beyond which some hysteresis becomes immanent in the ECG data (compare blue with red data in Figure 7). Specifically, the conductivity (Figure 7b) and the density of states (Figure 7a) at lower reductive potentials increase in the next cycle. These are indications for the beginning of an irreversible reduction at a potential of –2 V, which are further corroborated by the strong reductive peak at –1.83 V in the DPV measurements (Figure 6). Similar steps under reductive scanning have been observed by Carroll et al. for 2H-MoS_2 obtained by liquid exfoliation, however with much weaker signal intensity and substantially thicker films.[25] We suspect that sufficiently thin films and the high sensitivity of EMAS are necessary to observe these additional reductive processes. This is reflected by our thickness-dependent data in Figure 3 and Figure S7, Supporting Information, in which thinner film thicknesses lead to clearer trends in the reductive scans. Based on previous reductive experiments with 2H-MoS_2 in water, we hold either the reduction of Mo^{4+} ions or a phase transition to the 1T phase[35,45] as the most likely cause for the reduction at –2 V. Sulfur vacancies are often found in 2H-MoS_2[46] and n-type behavior (as found here) is attributed to such sulfur deficiency,[47] or more precisely, interstitial Mo or Mo occupying S sites.[48] Therefore, such interstitial or antisite Mo^{4+} is a likely candidate to be involved in the reduction at –2 V. This interpretation is supported by the increased conductivity in the ECG scans once a previous scan exceeded this threshold potential (Figure 7b). However, a phase transition to the metallic 1T allotrope would also explain the increase in conductivity.

For reductive potentials > |–2.3 V|, the decrease of all beforementioned EMAS features indicates the electrochemical degradation of the 2H-MoS_2 nanosheet films.

4. Conclusion

We have determined the electronic structure near the band gap of colloidal 2H-MoS_2 nanosheets with a thickness of 1–2 monolayers by a combination of EMAS, ECG, and DPV. We identified the edges of the conduction and valence band of the direct transition in the monolayers at –1.18 and 0.77 V versus Fc/Fc^+ respectively, yielding a band gap of 1.95 eV, that is, an excitonic binding energy of less than 0.1 eV in the high dielectric environment of 0.1 M *n*-Bu_4NPF_6/CH_3CN. For the bilayers, we found an indirect band gap of 1.55 eV with the valence band edge located at 0.37 V. The as-synthesized 2H-MoS_2 nanosheets are n-doped and show strong bandgap renormalization effects upon electrochemical oxidation and reduction. We identified two separate band nesting transitions that utilize points in the conduction band with roughly the same energy as the conduction band edge (–1.2 eV). While the oxidation of the valence band is irreversible, we find the reduction of the conduction band to be mostly reversible over a large potential range. These results indicate that colloidal chemistry affords high-quality 2H-MoS_2 nanosheets with a well-preserved electronic structure and potential applications in reductive electrocatalysis, for example, for the electrocatalytic hydrogen evolution reaction.

5. Experimental Section

Synthesis of 2H-MoS_2 Nanosheets: Colloidal 2H-MoS_2 nanosheets were synthesized based on the previously reported protocol[10,11] to obtain mono and bilayers with a lateral dimension of ≈20–25 nm. The Mo-precursor was prepared by dissolving molybdenum(V)-chloride in a mixture of oleylamine and oleic acid of 10:1 by stirring inside a glovebox for 2 days. The concentration of the precursor was set to 240 mM. For the nanosheet synthesis, elemental sulfur (87.5 mg, 2.73 mmol) and 17 mL oleylamine were added to a three-neck flask and degassed under vacuum from an oil pump for 30 min at 85 °C. During this step, the sulfur dissolved, and the solution turned dark. The flask was then put under inert gas (Argon) and HMDS (250 µL, 1.22 mmol) was added via a syringe before the reaction was heated to 320 °C. During the heating process, the solution changed color from dark brown to clear red.

After a constant temperature was reached, the molybdenum precursor (1.15 mL, 276 µmol) was added over 30 min using a syringe pump. After the first drops of precursor were added, a final color change to opaque black was immediately visible. The synthesis was continued at the same temperature for 30 min after the addition of the precursor and then quickly cooled to room temperature. After the reaction, the synthesized 2H-MoS_2 nanosheets were precipitated by the addition of 16 mL hexane and centrifugation at 3300 rcf for 10 min. The precipitate was redispersed in hexane and the centrifugation step was repeated two times. The entire precipitation was performed under inert conditions and the sample was then stored dispersed in hexane and under nitrogen.

Chemicals for Electrochemical Experiments: All chemicals used for electrochemical experiments were stored and handled under an inert atmosphere. Dry and degassed CH_3CN was obtained by three times distillation of HPLC-grade solvent over P_4O_{10} followed by three freeze-pump-thaw cycles. Afterward, the acetonitrile was stored over a 3 Å molecular sieve, which was activated at 220 °C and 2–3 mbar for 48 h beforehand. Prior to use, the electrolyte *n*-Bu_4NPF_6 (98%, Alfa Aesar) was recrystallized five times from 3:1 $EtOH/H_2O$ followed by drying at 105 °C and 2–3 mbar for 6 days. Purity was checked by ^1H-, ^{13}C-, ^{19}F-, and ^{31}P-NMR spectroscopy. Before preparing fresh electrolyte solutions for each experiment, the stored CH_3CN was run over a column of neutral alumina, priorly activated at 220 °C and 2–3 mbar for 6 days. $AgClO_4$ (≥97%, anhydrous, Alfa Aesar) and Ferrocene (98%, Acros Organics) were used without further purification.

Differential Pulse Voltammetry: DPV measurements were controlled by using a CHI760E Bipotentiostat (CH-Instruments). Experiments were performed in a glovebox under a nitrogen atmosphere and additionally, the used full-glass gas-tight electrochemical cell was placed in a faraday cage for better electrical shielding. A three-electrode arrangement was employed: A 3 mm diameter Pt disc electrode (Metrohm part no. 6.1204.310) as a working electrode, a 1 mm diameter coiled platinum wire as a counter electrode , and a Haber–Luggin double-reference electrode[49,50] composed of an Ag/Ag^+ system (1 mm diameter silver wire in a 0.01 M $AgClO_4$ solution in 0.1 M *n*-Bu_4NPF_6/CH_3CN) capacitively coupled (10 nF) to a Pt wire which was immersed into the electrolyte next to the capillary opening. To avoid any contamination of the electrolyte within the sample chamber by the reference electrode solution, or vice versa, an additional frit filled with 0.1 M *n*-Bu_4NPF_6/CH_3CN was inserted between the Haber–Luggin capillary and the reference electrode compartment.

Measurements were carried out starting at the OCP of the bare Pt electrode of –0.2 V versus Ag/Ag^+ to –2.8 V in reductive, and to 2 V in oxidative direction. Scans were performed with a potential step width of 4 mV, 50 mV amplitude, 0.06 s pulse width, 0.02 s sampling width, and a 0.5 s pulse period at a measurement sensitivity of 10 µA V^{-1}. DPV measurements were iR-compensated by the integrated positive feedback function of the CHI760E. The potential values of all measurement data were converted to the formal potential of the external redox couple Ferrocene/Ferrocenium (Fc/Fc^+), which was measured at 0.082 V versus Ag/Ag^+ within the same setup used for DPV measurements.

The sample chamber of the electrochemical cell was filled with 12 mL of 0.1 M *n*-Bu_4NPF_6/CH_3CN. At first, background electrolyte scans were performed with a freshly polished Pt disc electrode. Afterward, 30 µL of a 10 mM 2H-MoS_2 solution in hexane were drop casted on the working electrode, dipped in a 3% ethane-1,2-dithiol solution in acetonitrile for a few minutes, and afterward, washed with acetonitrile. Then, sample measurements were performed five times in a row with the same parameters as for the respective background scan. Freshly prepared 2H-MoS_2 layers were either used for reductive or oxidative scans, not for both measurement directions.

Electrochemical Gating and Potential-Modulated Absorption Spectroscopy Sample Preparation: Before film preparation, both substrates used for ECG and EMAS were cleaned as follows: A Pt interdigitated electrode with a gap width of 5 µm (Metrohm G-IDEPT5) was rinsed several times with H_2O and MeOH. FTO-coated glass (Solaronix TCO22-15) was sonicated for 15 min each in acetone, hexane, and 10% solution of Extran MA01 (Merck) and H_2O. From here on, both substrates were treated identically. To ensure good contact with the substrate, not the entire substrate surfaces were coated, but mainly the part that is in contact with the electrolyte later on. (3-mercaptopropyl) trimethoxysilane (MPTMS) treatment was performed by placing the substrates in a stirred 3% MPTMS toluene solution at 50 °C for 90 min followed by rinsing with toluene. Afterward, the substrates were placed in a 4 mM 2H-MoS_2 nanosheet solution in hexane for 22 h, which was sonicated for 15 min beforehand. Film preparation happened by precipitation of the long-term unstable colloidal solution. For the thinner EMAS samples, the film preparation times were 30 min, 5 min, and 30 s. To further stabilize and interlink the prepared 2H-MoS_2 layers, the substrates were placed in a stirred solution of 3% ethane-1,2-dithiol in acetonitrile for 30 min followed by five times dipping in acetonitrile.

ECG Measurements: The measurement setup for ECG measurements was basically the same as for DPV scans. Measurements were performed under the same inert conditions in the same full-glass-cell with the same electrolyte solution, counter and reference electrode, only the working electrode was different: A beforehand mentioned Pt interdigitated electrode with a gap width of 5 µm between the electrode arrays and total channel length of 3.373 m (Metrohm G-IDEPT5) was used. Both arrays were independently controlled by the two working electrode channels of the CHI760E bipotentiostat. All measurements were initiated at the OCP at –0.4 V versus Fc/Fc^+. Before the 2H-MoS_2 nanosheet-coated interdigitated electrodes were measured, an uncoated

sample was investigated with the same parameters to check whether there were any contaminations in the electrolyte solution.

Differential capacitance was determined via chronoamperometry (CA) by measuring in 20 mV steps toward the respective reductive or oxidative direction. At each of these steps, which were applied to both working electrodes simultaneously, the current was detected over 5 s and the amount of flowed charge was determined via integration. The capacitive current was extracted from the total measured current by background correction (assuming the Faraday current exhibits Cottrell behavior). At the end of such a 20 mV step, the final potential was held and the steady-state conductivity was measured by means of CV. The potential of the first working electrode was held constant while the potential of the second working electrode was scanned ±10 mV around this constant potential. In case a conductive channel was present between both working electrode, the current detected on both working electrode channels was the same magnitude, but had different signs. The steady-state conductivity was calculated from the slopes of the *iV*-curves. Then, the next 20 mV step was applied to both working electrode by means of CA, and the differential capacitance was calculated again, and so on. This combination of CA and CV was done until the final reductive or oxidative potential was reached. Then, the scan direction was reversed and measurements back to the OCP were performed. The accumulated charge was calculated by integrating the differential capacitances until the potential of interest.

CA measurements were performed in 20 mV steps with a 5 s pulse width and 1 ms sample interval. CV measurements were conducted with a scan rate of 10 mV s^{-1} and a 1 mV sample interval. The measurement sensitivity of both techniques was set to 10 µA V^{-1}. As for DPV, all CA and CV measurements were iR-compensated, and the potentials were converted to the Fc/Fc^+ redox couple as described above.

EMAS-Measurements: A detailed schematic illustration of the EMAS setup, including the model number of each component, is shown in Figure S15, Supporting Information. For EMAS measurements, a home-built spectroelectrochemical transmission cell, equipped with a 1 mm diameter Ag wire pseudoreference electrode, a 1 mm diameter coiled platinum wire counter electrode, and a fFTO-coated glass as the working electrode were used. The working electrode was either coated with 2H-MoS_2 nanosheets as described above or uncoated for reference measurements. The measurement cell was filled with 6 mL 0.1 M *n*-Bu_4NPF_6/CH_3CN and assembled within a glovebox. For the actual measurements, it was afterward transferred outside of the box and placed in a faraday cage.

Using the CHI760E bipotentiostat, a constant potential at the OCP of approximately –0.5 V versus Fc/Fc^+ was applied to the working electrode. Then, a rectangular-shaped modulated potential, produced by a Waveform generator (PSG9080, Joy-IT), with a modulation frequency of 37 Hz and a variable amplitude as an offset was superimposed. Meanwhile, the working electrode was transilluminated by monochromatic light generated by an Apex2 QTH lamp (Oriel Instruments) and selected using a Cornerstone 130 (Oriel Instruments) monochromator. Above 600 nm, a 570 nm long-pass filter was introduced into the beam path to block components with a higher diffraction order. The transmitted light was detected at a DET36A Si-biased detector (Thorlabs), and the signal was passed to an MFLI lock-in amplifier (Zurich Instruments). In parallel, the lock-in amplifier received the modulated potential generated by the signal generator as a reference signal and searched for a modulated component in the optical signal that oscillated at the same frequency. Considering the phase relationship between the modulated potential and the modulated component in the optical signal, it was determined whether the measured signal was an induced absorption or a bleach (see Figure S1, Supporting Information, and the accompanied text).

During the EMAS measurement, the modulated potential component was applied to the sample in such a way that the total potential signal always oscillated between OCP and a corresponding reductive or oxidative potential. At the beginning of the measurement, the peak-to-peak amplitude was 60 mV. With an appropriate offset, the signal was then shifted to positive or negative values, so that the potential was then modulated between OCP and OCP ±60 mV. At this potential, a complete spectrum from 350 to 860 nm was scanned in 3 nm steps. Afterward, the peak-to-peak amplitude was increased by 60 mV, the signal offset was adjusted accordingly, and a complete spectrum was recorded again. This was done until the final corresponding oxidative or reductive potential was reached and a complete data set was recorded.

During the EMAS measurement, iR-compensation by the integrated positive feedback function of the CHI760E was activated and the measurement sensitivity of the bipotentiostat was set to 0.1 mA V^{-1}. The AC-coupled signal input of the lock-in amplifier was set to 10 MΩ with an input range of 10 mV. Incoming signals were processed by a 6th-order low-pass filter having a time constant of 100 ms. The resolution of the monochromator was set to 3–4 nm by adjusting the input and output slit width. The potential of the measured data was also converted to the formal potential of the external redox couple Ferrocene/Ferrocenium (Fc/Fc^+), which was measured at 0.32 V versus Ag pseudoreference electrode within the same setup.

Other Experimental Techniques: UV–vis spectra were recorded using a Cary 5000 UV–vis-NIR spectrophotometer from Agilent Technologies. As samples, the 2H-MoS_2 nanosheet-coated FTO windows, previously employed for EMAS measurements, were used. The same samples were also used for SEM measurements that were performed using a Hitachi SU 8030. Information about the height of the 2H-MoS_2 nanosheet films on FTO glass and Pt-interdigitated electrode substrates was obtained using a Bruker Dektak XT-A stylus profilometer measuring over the edge of the film coating over a distance of 1000 µm using a tipforce of 1 mg. For identifying the layer thickness and the lateral size of the 2H-MoS_2 nanosheets, the colloidal solution was dropcast onto a carbon-coated copper grid (Quantifoil) and measured by TEM with a Tecnai G2 F20 TMP microscope (FEI) with an acceleration voltage of 200 kV.

Supporting Information

Supporting Information is available from the Wiley Online Library or from the author.

Acknowledgements

The authors thank André Niebur, excellence cluster PhoenixD, and the Institute of Physical Chemistry and Electrochemistry, Hannover for performing TEM measurements. Distilled solvents used for electrochemical experiments were kindly provided by Florian Fetzer and Andreas Schnepf, Institute of Inorganic Chemistry, University of Tübingen. The authors thank Elke Nadler, Institute of Physical and Theoretical Chemistry, University of Tübingen, for performing SEM/EDX measurements using a Hitachi SU 8030 SEM, which was funded by the DFG under the contract INST 37/829-1 FUGG. The glass and metal workshops of the Central Chemistry Institute, University of Tübingen, are acknowledged for the fabrication of many components used in the measurement setups. J.L. is thankful for funding from the Deutsche Forschungsgemeinschaft (DFG, German Research Foundation) under Germany's Excellence Strategy within the Cluster of Excellence PhoenixD (EXC2122, Project ID 390833453). Financial support for this work was provided by the European Research Council (ERC) under the European Union's Horizon 2020 research and innovation program (grant agreement No 802822), as well as the DFG under grant SCHE1905/9-1.

Open access funding enabled and organized by Projekt DEAL.

Conflict of Interest

The authors declare no conflict of interest.

Data Availability Statement

The data that support the findings of this study are available from the corresponding author upon reasonable request.

Keywords

colloidal synthesized 2H-MoS_2, differential pulse voltammetry, potential-dependent conductivity, potential-modulated absorption spectroscopy, thin films

Received: November 15, 2022
Revised: February 3, 2023
Published online: March 9, 2023

[1] D. Lembke, S. Bertolazzi, A. Kis, *Acc. Chem. Res.* **2015**, *48*, 100.
[2] Y. Sun, S. Gao, F. Lei, Y. Xie, *Chem. Soc. Rev.* **2015**, *44*, 623.
[3] A. Kuc, in *Chemical Modelling*, (Eds: M. Springborg, J.-O. Joswig), Royal Society Of Chemistry, London **2014**, p. 1.
[4] T. Cheiwchanchamnangij, W. R. L. Lambrecht, *Phys. Rev. B* **2012**, *85*, 205302.
[5] H. Li, J. Wu, Z. Yin, H. Zhang, *Acc. Chem. Res.* **2014**, *47*, 1067.
[6] C. Backes, R. J. Smith, N. McEvoy, N. C. Berner, D. McCloskey, H. C. Nerl, A. O'Neill, P. J. King, T. Higgins, D. Hanlon, N. Scheuschner, J. Maultzsch, L. Houben, G. S. Duesberg, J. F. Donegan, V. Nicolosi, J. N. Coleman, *Nat. Commun.* **2014**, *5*, 4576.
[7] X. Wang, H. Feng, Y. Wu, L. Jiao, *J. Am. Chem. Soc.* **2013**, *135*, 5304.
[8] C. Muratore, J. J. Hu, B. Wang, M. A. Haque, J. E. Bultman, M. L. Jespersen, P. J. Shamberger, M. E. McConney, R. D. Naguy, A. A. Voevodin, *Appl. Phys. Lett.* **2014**, *104*, 261604.
[9] D. Son, S. I. Chae, M. Kim, M. K. Choi, J. Yang, K. Park, V. S. Kale, J. H. Koo, C. Choi, M. Lee, J. H. Kim, T. Hyeon, D.-H. Kim, *Adv. Mater.* **2016**, *28*, 9326.
[10] A. Niebur, A. Söll, P. Haizmann, O. Strolka, D. Rudolph, K. Tran, F. Renz, A. P. Frauendorf, J. Hübner, H. Peisert, M. Scheele, J. Lauth, *Nanoscale* **2023**, Accepted Manuscript, https://doi.org/10.1039/D3NR00096F
[11] A. P. Frauendorf, A. Niebur, L. Harms, S. Shree, B. Urbaszek, M. Oestreich, J. Hübner, J. Lauth, *J. Phys. Chem. C* **2021**, *125*, 18841.
[12] G. Pippia, A. Rousaki, M. Barbone, J. Billet, R. Brescia, A. Polovitsyn, B. Martín-García, M. Prato, F. De Boni, M. M. Petrić, A. B. Mhenni, I. Van Driessche, P. Vandenabeele, K. Müller, I. Moreels, *ACS Appl. Nano Mater.* **2022**, *5*, 10311.
[13] C. B. Murray, D. J. Norris, M. G. Bawendi, *J. Am. Chem. Soc.* **1993**, *115*, 8706.
[14] S. Hwangbo, L. Hu, A. T. Hoang, J. Y. Choi, J.-H. Ahn, *Nat. Nanotechnol.* **2022**, *17*, 500.
[15] M.-L. Tsai, S.-H. Su, J.-K. Chang, D.-S. Tsai, C.-H. Chen, C.-I. Wu, L.-J. Li, L.-J. Chen, J.-H. He, *ACS Nano* **2014**, *8*, 8317.
[16] A. Y. S. Eng, A. Ambrosi, Z. Sofer, P. Šimek, M. Pumera, *ACS Nano* **2014**, *8*, 12185.
[17] M. Timpel, G. Ligorio, A. Ghiami, L. Gavioli, E. Cavaliere, A. Chiappini, F. Rossi, L. Pasquali, F. Gärisch, E. J. W. List-Kratochvil, P. Nozar, A. Quaranta, R. Verucchi, M. V. Nardi, *npj 2D Mater. Appl.* **2021**, *5*, 64.
[18] C. Zhang, A. Johnson, C.-L. Hsu, L.-J. Li, C.-K. Shih, *Nano Lett.* **2014**, *14*, 2443.
[19] C. Wang, M. Shim, P. Guyot-Sionnest, *Appl. Phys. Lett.* **2002**, *80*, 4.
[20] S. C. Boehme, H. Wang, L. D. A. Siebbeles, D. Vanmaekelbergh, A. J. Houtepen, *ACS Nano* **2013**, *7*, 2500.
[21] T. J. Jacobsson, T. Edvinsson, *J. Phys. Chem. C* **2012**, *116*, 15692.
[22] S. G. Hickey, D. J. Riley, E. J. Tull, *J. Phys. Chem. B* **2000**, *104*, 7623.
[23] D. Spittel, J. Poppe, C. Meerbach, C. Ziegler, S. G. Hickey, A. Eychmüller, *ACS Nano* **2017**, *11*, 12174.
[24] D. Vanmaekelbergh, A. J. Houtepen, J. J. Kelly, *Electrochim. Acta* **2007**, *53*, 1140.
[25] G. M. Carroll, H. Zhang, J. R. Dunklin, E. M. Miller, N. R. Neale, J. van de Lagemaat, *Energy Environ. Sci.* **2019**, *12*, 1648.
[26] S. S. Ataei, A. Sadeghi, *Phys. Rev. B* **2021**, *104*, 155301.
[27] M. Weber, S. Westendorf, B. Märker, K. Braun, M. Scheele, *Phys. Chem. Chem. Phys.* **2019**, *21*, 8992.
[28] C. M. Cardona, W. Li, A. E. Kaifer, D. Stockdale, G. C. Bazan, *Adv. Mater.* **2011**, *23*, 2367.
[29] J. K. Ellis, M. J. Lucero, G. E. Scuseria, *Appl. Phys. Lett.* **2011**, *99*, 261908.
[30] A. Chernikov, A. M. van der Zande, H. M. Hill, A. F. Rigosi, A. Velauthapillai, J. Hone, T. F. Heinz, *Phys. Rev. Lett.* **2015**, *115*, 126802.
[31] P. Schiettecatte, P. Geiregat, Z. Hens, *J. Phys. Chem. C* **2019**, *123*, 10571.
[32] E. A. A. Pogna, M. Marsili, D. De Fazio, S. Dal Conte, C. Manzoni, D. Sangalli, D. Yoon, A. Lombardo, A. C. Ferrari, A. Marini, G. Cerullo, D. Prezzi, *ACS Nano* **2016**, *10*, 1182.
[33] K. P. Dhakal, D. L. Duong, J. Lee, H. Nam, M. Kim, M. Kan, Y. H. Lee, J. Kim, *Nanoscale* **2014**, *6*, 13028.
[34] D. Van Tuan, B. Scharf, Z. Wang, J. Shan, K. F. Mak, I. Žutić, H. Dery, *Phys. Rev. B* **2019**, *99*, 085301.
[35] S. Wu, Z. Zeng, Q. He, Z. Wang, S. J. Wang, Y. Du, Z. Yin, X. Sun, W. Chen, H. Zhang, *Small* **2012**, *8*, 2264.
[36] A. Ambrosi, Z. Sofer, M. Pumera, *Small* **2015**, *11*, 605.
[37] M. Z. M. Nasir, Z. Sofer, A. Ambrosi, M. Pumera, *Nanoscale* **2015**, *7*, 3126.
[38] J. Ryou, Y.-S. Kim, S. Kc, K. Cho, *Sci. Rep.* **2016**, *6*, 29184.
[39] L. G. Gagliardi, C. B. Castells, C. Ràfols, M. Rosés, E. Bosch, *J. Chem. Eng. Data* **2007**, *52*, 1103.
[40] A. Carvalho, R. M. Ribeiro, A. H. Castro Neto, *Phys. Rev. B* **2013**, *88*, 115205.
[41] J. Kopaczek, S. J. Zelewski, M. P. Polak, A. Gawlik, D. Chiappe, A. Schulze, M. Caymax, R. Kudrawiec, *J. Appl. Phys.* **2019**, *125*, 135701.
[42] J. Hong, M. Koshino, R. Senga, T. Pichler, H. Xu, K. Suenaga, *ACS Nano* **2021**, *15*, 7783.
[43] J. E. Padilha, H. Peelaers, A. Janotti, C. G. Van de Walle, *Phys. Rev. B* **2014**, *90*, 205420.
[44] K. F. Mak, K. He, C. Lee, G. H. Lee, J. Hone, T. F. Heinz, J. Shan, *Nat. Mater.* **2013**, *12*, 207.
[45] G. Gao, Y. Jiao, F. Ma, Y. Jiao, E. Waclawik, A. Du, *J. Phys. Chem. C* **2015**, *119*, 13124.
[46] C. Tsai, H. Li, S. Park, J. Park, H. S. Han, J. K. Nørskov, X. Zheng, F. Abild-Pedersen, *Nat. Commun.* **2017**, *8*, 15113.
[47] S. McDonnell, R. Addou, C. Buie, R. M. Wallace, C. L. Hinkle, *ACS Nano* **2014**, *8*, 2880.
[48] M.-H. Shang, H. Hou, J. Zheng, Z. Yang, J. Zhang, S. Wei, X. Duan, W. Yang, *J. Phys. Chem. Lett.* **2018**, *9*, 6032.
[49] B. Gollas, B. Krauß, B. Speiser, H. Stahl, *Curr. Sep.* **1994**, *13*, 42.
[50] A. W. Bott, *Curr. Sep.* **1995**, *14*, 64.